Exchange Interactions and Covalency in Dinuclear Complexes of Iron(III) and Gallium(III) Containing the Redox-Noninnocent Ligand 1,2-Bis(3,5-di-*tert*-butyl-2-hydroxyphenyl)oxamide

Udo Beckmann,[a] Eckhard Bill,[a] Thomas Weyhermüller,[a] and Karl Wieghardt*[a]

Keywords: Iron / Gallium / EPR spectroscopy / Moessbauer spectroscopy / Radicals / Magnetic properties / Exchange interactions

The dinucleating ligand 1,2-bis(3,5-di-*tert*-butyl-2-hydroxyphenyl)oxamide [H_4(bbpo)] has been synthesized. From its reaction with $GaCl_3$ or $FeCl_3$ in CH_3OH/NaOH the salts $[N(nBu)_4]_2[M_2^{III}(bbpo)Cl_4]$ [M = Ga (**1**), Fe (**2**)] have been isolated as crystalline solids upon addition of $[N(nBu)_4]Cl$. Complexes **1** and **2** have been characterized by single-crystal X-ray crystallography. Cyclic voltammetry established that both species undergo two successive, reversible one-electron oxidations in CH_2Cl_2 {0.10 M $[N(nBu)_4]PF_6$} which are shown to be ligand-centered: one and then two *N*,*O*-coordinated *o*-iminobenzosemiquinonate π-radicals form which couple antiferromagnetically with the high-spin ferric ions in **2**. Thus, the monoanion of **2** has an $S_t = {}^1/_2$ ground state. The complexes have been characterized by Mössbauer, UV/Vis, and EPR spectroscopy.

1. Introduction

In a recent series of publications[1−6] we have shown that *o*-aminophenolates and their ring-substituted derivatives are redox-noninnocent ligands in coordination chemistry. In particular, we established that high-quality X-ray crystallography allows the unequivocal determination of the protonation and oxidation level of a given *N*,*O*-coordinated ligand in a transition metal complex and that it is possible to discern between an *N*,*O*-coordinated *o*-iminophenolate(−), $(L^{IP})^{2-}$, and its one-electron oxidized form, the *o*-iminobenzosemiquinonate(1−) π-radical, $(L^{ISQ})^{-}$.

When such a radical ligand ($S_{rad} = {}^1/_2$) is coordinated to a paramagnetic transition metal ion with an incompletely filled t_{2g} subshell, very strong intramolecular antiferromagnetic exchange coupling between the radical spin and the t_{2g}^n configuration is observed. Thus, $[Cr^{III}(L^{ISQ})_3]$,[3] containing a Cr^{III} ion with t_{2g}^3 configuration and three $(L^{ISQ})^{1-\cdot}$ radical anions, possesses an $S_t = 0$ ground state, whereas its cobalt(III) analogue[1] (t_{2g}^6) possesses an $S_t = {}^3/_2$ ground state because the three ligand spins couple ferromagnetically.

Here we describe the synthesis of a new dinucleating ligand that contains two *o*-aminophenolate units, which, in principle, should be oxidizable to two *o*-iminobenzosemiquinonate units. The ligand is the tetraanion of 1,2-bis(3,5-di-*tert*-butyl-2-hydroxyphenyl)oxamide [H_4(bbpo)], shown in Scheme 1. If both bound metal ions are paramagnetic, e.g. high-spin Fe^{III}, exchange coupling between these ions and the ligand π-radicals and coupling between the two metal ions containing units, which are bridged by an oxamide unit, should lead to various ground states. As we will show here, this is indeed the case.

[a] Max-Planck-Institut für Strahlenchemie,
Stiftstrasse 34−36, 45470 Mülheim an der Ruhr, Germany

2. Results and Discussion

2.1. Synthesis and Characterization of Complexes 1 and 2

The reaction of 3,5-di-*tert*-butyl-2-(hydroxyamino)benzene (2 equiv.) [7] with oxalyl chloride (1 equiv.) in diethyl ether in the presence of the base triethylamine (2 equiv.) affords the ligand 1,2-bis(3,5-di-*tert*-butyl-2-hydroxyphenyl)oxamide [H_4(bbpo)] in good yields (Scheme 1).

From the reaction of deprotonated H_4(bbpo) in CH_3OH/NaOH solution and 2 equiv. of $GaCl_3$ or $FeCl_3$ the yellow and green crystalline salts of $[N(nBu)_4]_2[M_2^{III}(bbpo)Cl_4]$ [M = Ga^{III} (**1**), Fe^{III} (**2**), respectively] were obtained upon addition of $[N(nBu)_4]Cl$.

In accord with the structures shown in Scheme 1 for the dianions of **1** and **2** the infrared spectra do not show ν(N−H) or ν(OH) stretching frequencies but prominent ν(C=O) stretching frequencies at 1633 cm^{-1} for **1** and at 1611 cm^{-1} for **2**.

The electro spray mass spectra of **1** and **2** in CH_3OH in the negative ion detection mode display peaks at $m/z = 737$ for **1** and at $m/z = 709$ for **2**, corresponding to the monoanions $[M_2^{III}(bbpo)Cl_3]^-$ (M = Ga, Fe, respectively). Both peaks display the correct isotope pattern.

Our attempts to synthesize a pure sample of the paramagnetic heterodinuclear complex $[N(nBu)_4]_2[Ga^{III}$-

  DOI: 10.1002/ejic.200200516

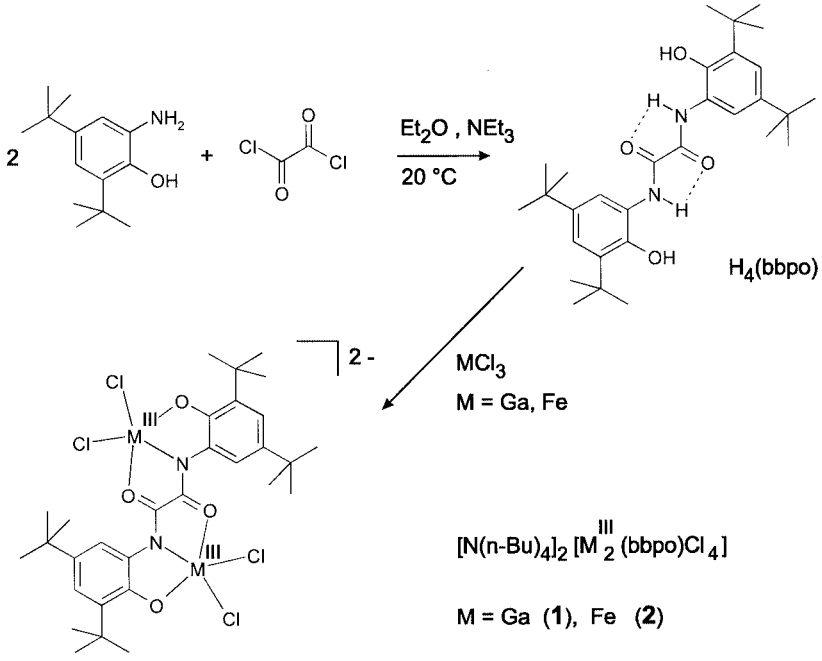

Scheme 1

$Fe^{III}(bbpo)Cl_4$], which would reveal the rhombicity, *E*/*D*, of a single high-spin ferric site in its EPR spectrum, yielded samples contaminated by **1** and **2**. Nevertheless, we found that in equimolar methanolic solutions of **1** [the pure gallium(III) species] and $FeCl_3$ the heterodinuclear species $[Ga^{III}Fe^{III}(bbpo)Cl_4]^{2-}$ is generated as well as **2**. The ESI (negative ion) mass spectra of such solutions clearly show the presence of $[GaFe(bbpo)Cl_3]^-$ at m/z = 724 (Z = 1) and of $[GaFe(bbpo)Cl_4]^{2-}$ at m/z = 379.5 (Z = 2). Both peaks display the correct isotope pattern. The signals of the corresponding homodinuclear monoanions $[M_2^{III}(bbpo)Cl_3]^-$ (M = Ga and Fe) are also present. Addition of $[N(nBu)_4]Cl$ to such solutions initiated the precipitation of a mixture of **1**, **2**, and $[N(nBu)_4]_2$ $[GaFe(bbpo)Cl_4]$. The latter is isomorphous and isostructural with **1** and **2** as was established by X-ray crystallography of a hand-picked, brown single crystal that contained a Ga/Fe ratio of ca. 1:1 (X-ray fluorescence analysis).

2.2. Crystal Structures of 1 and 2

The crystal structures of **1** and **2** have been determined at 100(2) K by single-crystal X-ray crystallography using

Table 1. Crystallographic data for **1**, and **2**

	1	**2**
Empirical formula	$C_{62}H_{112}Cl_4Ga_2N_4O_4$	$C_{62}H_{112}Cl_4Fe_2N_4O_4$
Formula mass	1258.80	1231.06
Space group	$P2_1/c$, no. 14	$P2_1/c$, no. 14
a [Å]	15.493(2)	15.3419(12)
b [Å]	14.182(2)	14.3702(10)
c [Å]	17.059(3)	17.1730(14)
β [°]	111.57(2)	112.29(2)
V [Å]	3485.7(9)	3503.2(5)
Z	2	2
T [K]	100(2)	100(2)
$\rho_{calcd.}$ [g cm^{-3}]	1.199	1.167
Diffractometer used	Nonius Kappa-CCD	Nonius Kappa-CCD
Refl. collected/$2\theta_{max}$ [°]	41071/50.00	60418/60.00
Unique refl./[$I > 2\sigma(I)$]	6137/5087	10221/7783
No. of param./restraints	343/3	382/16
μ(Mo-K_α) [cm^{-1}]	9.70	6.10
$R1$[a]/goodness of fit[b]	0.0945/1.238	0.0465/1.024
$wR2$[c] [$I > 2\sigma(I)$]	0.1982	0.1247

[a] Observation criterion: [$I > 2\sigma(I)$]. $R1 = \Sigma||F_o| - |F_c||/\Sigma|F_o|$. [b] GooF = $\{\Sigma[w(F_o^2 - F_c^2)^2]/(n - p)\}^{1/2}$. [c] $wR2 = \{\Sigma[w(F_o^2 - F_c^2)^2]/\Sigma[w(F_o^2)^2]\}^{1/2}$ where $w = 1/\sigma^2(F_o^2) + (aP)^2 + bP$ and $P = (F_o^2 + 2F_c^2)/3$.

Mo-K_α radiation. Table 1 gives crystallographic data and Table 2 summarizes selected bond lengths and angles. Figure 1 shows the structure of the dianion in crystals of **2**; the structure of **1** is very similar and not shown.

Table 2. Selected bond lengths [Å] and angles [°] of the dianions in crystals of **1** and **2**

	1	**2**
M−O1	1.921(5)	1.929(2)
M−O2	2.110(5)	2.080(2)
M−Cl1	2.205(2)	2.253(1)
M−Cl2	2.198(2)	2.246(1)
M−N1	1.969(6)	2.049(2)
N1−C7	1.308(9)	1.310(2)
N1−C6	1.402(9)	1.403(2)
O1−C1	1.350(9)	1.340(2)
O2−C7	1.268(8)	1.273(2)
C1−C2	1.41(1)	1.414(3)
C1−C6	1.42(1)	1.414(2)
C2−C3	1.39(1)	1.394(3)
C3−C4	1.39(1)	1.401(3)
C4−C5	1.38(1)	1.391(3)
C5−C6	1.39(1)	1.387(3)
C7−C7*	1.50(1)	1.509(4)
O1−M−N1	83.3(2)	78.8(1)
O1−M−O2*	161.8(2)	154.9(1)
N1−M−O2*	79.5(2)	77.9(1)
O1−M−Cl2	96.6(2)	96.9(1)
N1−M−Cl2	129.1(2)	133.6(1)
O2*−M−Cl2	89.6(1)	92.5(1)
O1−M−Cl1	100.9(2)	101.5(1)
N1−M−Cl1	114.0(2)	108.2(1)
O2*−M−Cl1	91.6(2)	94.5(1)
Cl2−M−Cl1	115.9(1)	117.82(2)

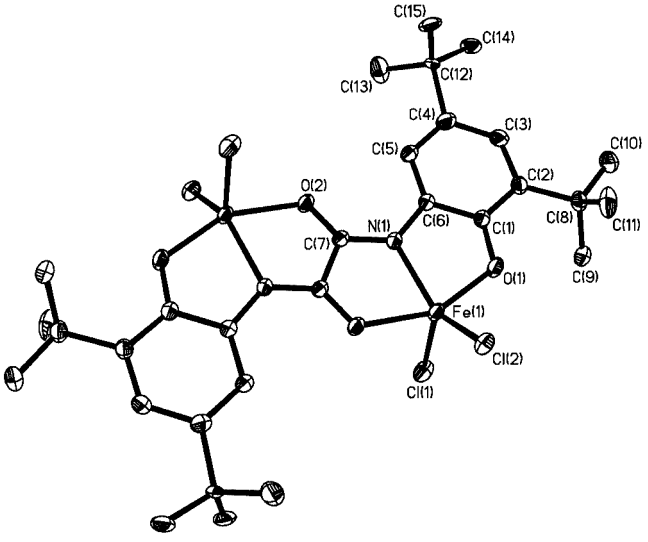

Figure 1. ORTEP representation of the structure of the dianion $[Fe^{III}_2(bbpo)Cl_4]^{2-}$ in crystals of **2**; that of the dianion in **1** is similar and not shown.

Both structures consist of well-separated tetra-*n*-butylammonium cations and dinuclear dianions (ratio 2:1).

The metal ions Ga^{III} and Fe^{III} in **1** and **2**, respectively, are five-coordinate with a distorted trigonal-bipyramidal MCl_2NO_2 polyhedron, where the two chloride ions and the nitrogen donor N1 occupy basal positions whereas the two oxygen donors O1 and O2 are in the remaining two axial sites. The Fe−Cl, Fe−N and Fe−O bond lengths are quite long and indicate a high-spin d^5 configuration at the ferric ions in **2**. The corresponding bonds in **1** are similar since the ionic radii of five-coordinate Ga^{III} and high-spin Fe^{III}, 0.69 and 0.72 Å, respectively, are also similar.[9]

We note that the metrical details of the coordinated *o*-aminophenolate parts of the ligand $(bbpo)^{4-}$ clearly indicate the presence of two *N*,*O*-coordinated *o*-iminophenolato(2−) halves.[5] The six C−C bond lengths of the phenyl rings are, within experimental error, equidistant; no evidence for a quinoid-type distortion typical for *o*-iminobenzosemiquinonato(1−) π-radicals was detected.[1−6] Similarly, the C1−O1 bonds at ca. 1.35 Å are long and typical for phenolates. The two corresponding C6−N1 bonds at 1.40 Å are also long, indicating single bonds.

2.3. Magnetic Properties of 2

The diiron complex **2** has been studied by magnetometry and applied-field Mössbauer spectroscopy. In contrast to the diamagnetic digallium analog **1**, which shows a "normal" ^{1}H NMR spectrum without paramagnetically shifted lines (see Exp. Sect.), the iron compound has a substantial magnetic moment at ambient temperature. Figure 2 (top) displays the temperature dependence of the magnetic moment of solid **2** recorded in the range 2−300 K using a SQUID magnetometer and an external field of 1 T. The molar susceptibilities were corrected for underlying diamagnetism by use of tabulated Pascal constants ($\chi_{dia} = -825 \times 10^{-6}$ cm^3·mol^{-1}). The magnetic moment decreases monotonically from ca. 7 μ_B at 300 K to about 0.5 μ_B at 4 K. The solid line in Figure 2 represents a best fit of the data using the spin Hamiltonian in Equation (1) with $S_1 = S_2 = {}^5/_2$, $J = -9.7 \pm 0.5$ cm^{-1}, $g = 2.016$, $|D| = 1.6 \pm 0.3$ cm^{-1}, and $E/D = 0.33$ for both identical iron sites.

$$H = -2J\,\vec{S}_1 \cdot \vec{S}_2 + \sum_{i=1,2}\{D_i[S^2_{z,i} - \tfrac{1}{3}S_i(S_i+1) + {}^{E}\!/_{D}(S^2_{x,i} - S^2_{y,i})] + g_i\mu_B\vec{S}_i \cdot \vec{B}\} \quad (1)$$

Thus, the spins of the two ferric ions in **2** are weakly antiferromagnetically coupled; the complex possesses an EPR-silent $S_t = 0$ ground state which, however, is not very well isolated from paramagnetic excited states. Thus, the applied field can induce a weak magnetic moment even at 2 K. This is best observed in multi-field measurements with variable-temperature data sampled on a $1/T$ scale (inset of Figure 2). The increasing level of magnetization with increasing field at low temperatures (arrows in the inset) indicates multiplet-mixing by competing exchange and single-ion zero-field splitting (ZFS). Increasing temperature (to the left in the inset) leads to Boltzmann population of the excited S = 1, 2 states and increasing magnetization. The decline of M_{mol} below $\mu_B B/kT = 0.1$ represents the usual $1/T$ behavior

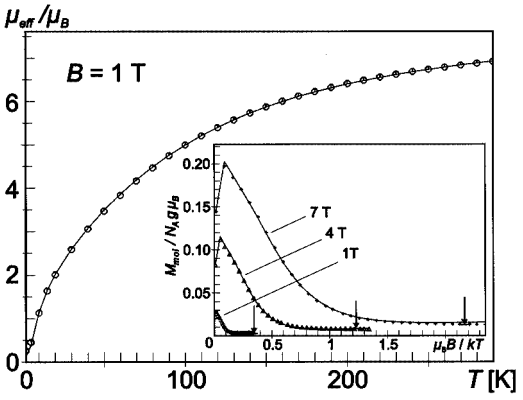

Figure 2. Temperature dependence of the magnetic moment, μ_{eff}, of **2** measured at $B = 1$ T; inset: variable-temperature variable-field plot of magnetization of **2**; the arrows indicate the induced magnetization of "$S_t = 0$" at low temperatures; see text for simulation parameters (solid lines)

at high temperatures due to equal population of the magnetic M_s sublevels. Systematic simulations of the temperature dependence at multiple fields yields a sensitive and unique measure of the exchange coupling constant, $J = -9.7 \pm 0.5$ cm^{-1}, and the ZFS parameter, $|D| = 1.6 \pm 0.3$ cm^{-1}. A similar but weaker antiferromagnetic coupling has been reported for the μ-oxalato-bridged dinuclear species $[Fe^{III}_2(\mu\text{-ox})(ox)_4]^{4-}$, with J established as -3.3 cm^{-1}.[8] The rhombicity parameter E/D in the analysis above was taken from an X-band EPR spectrum of the mixed-metal in complex $[Ga^{III}Fe^{III}(bbpo)Cl_4]^{2-}$ in CH_3OH solution, which selectively probes the Fe^{III} moiety in the bbpo ligand. The spectrum measured at 15 K shows the $g = 4.27$ signal (Figure 3) that is typical of Fe^{III}, $S = {}^5/_2$ with full rhombicity, $E/D = 0.33$. Note that at 15 K both "contaminants" of the Ga/Fe complex, **1** and **2**, are EPR-silent.

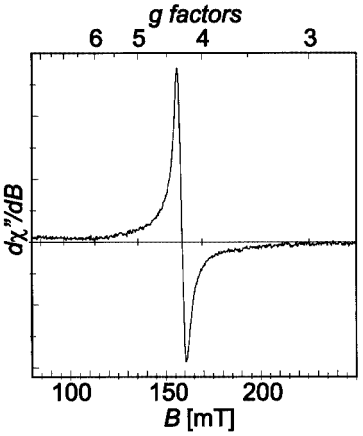

Figure 3. X-band EPR spectrum of $[Ga^{III}Fe^{III}(bbpo)Cl_4]^{2-}$ in CH_3OH solution at 15 K (conditions: frequency 9.4637 GHz; power 20.1 μW; modulation frequency 100 kHz; modulation amplitude 2.49 mT)

The zero-field Mössbauer spectrum of solid **2** at 80 K displays an asymmetric doublet with an isomer shift of 0.45 mm·s^{-1} and a quadrupole splitting of 0.97 mm·s^{-1} that are typical for high-spin ferric ions (Figure 4, top). The lines are broadened by residual spin relaxation close to the limit of fast rates. Magnetically perturbed spectra recorded at 1.8 K with fields of 3 and 7 T applied perpendicular to γ (Figure 4, center and bottom) show almost diamagnetic appearances, as expected for an electronic $S_t = 0$ ground state. The presence of induced magnetization can be visualized from the small but significant deviation of a diamagnetic simulation with "$S = 0$" from experiment (dotted lines). A spin Hamiltonian simulation based on Equation (1) with the above parameters gives a slightly better fit of the 3 and 7 T measurements. As expected, the small internal field in the latter case is opposite to the applied field. The corresponding Mössbauer parameters are summarized in Table 3.

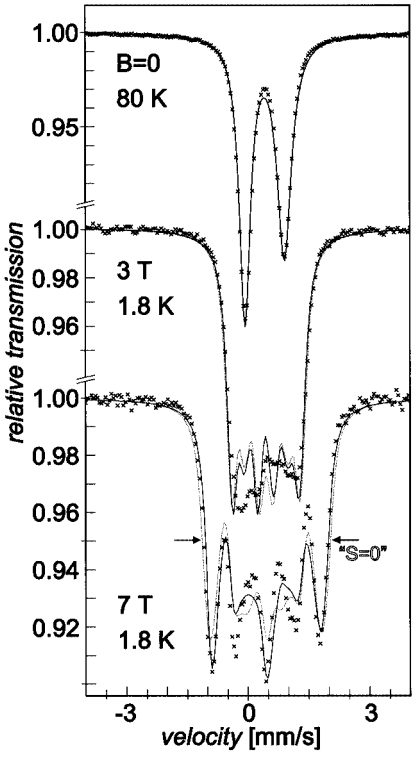

Figure 4. Zero- and applied-field Mössbauer spectra of solid **2**; parameters of the spin-Hamiltonian simulations based on Equation (1) (solid lines) are given in Table 3; the dotted lines represent an alternative diamagnetic simulation ($S = 0$) with the same electric hyperfine parameters

Hence, the magnetic Mössbauer spectra also demonstrate the effect of competing ZFS and exchange interaction for the low-lying spin multiplets of **2**. In addition, the symmetry of the splitting pattern reveals a large asymmetry parameter, $\eta = 0.9 \pm 0.1$, for the electric field gradient (efs) tensor, in agreement with the large rhombicity of the sites. The Mössbauer data agree fully with the electronic structure of **2** consisting of two identical, antiferromagnetically coupled high-spin ferric ions.

2.4. Electro- and Spectroelectrochemistry

The cyclic voltammograms (CV) of complexes **1** and **2** were recorded at 20 °C in CH_2Cl_2 solutions (0.10 M

Table 3. Mössbauer and spin Hamiltonian parameters for the di- and monoanion of **2**

	$[Fe^{III}_2(bbpo)Cl_4]^{2-}$	$[Fe^{III}_2(bbpo^{ox1})Cl_4]^{1-}$	
		Fe^1	Fe^2
S_{Fe} [a]	$^5/_2$, $^5/_2$	$^5/_2$	$^4/_2$
S_t [b]	0	$^1/_2$	
δ [mm·s^{-1}] at 4.2 K[c]	0.45	0.45	0.49
ΔE_Q [mm·s^{-1}] at 4.2 K[d]	0.98	0.98	−1.15
Γ [mm·s^{-1}] at 4.2 K[e]	0.28	0.28	0.28
$A_{exp}/g_N\beta_N$ [T][f]	21.35	21.35	(21.71, 22.2, 21.67)
$A_{local}/g_N\beta_N$ [T][f]	21.35	21.35	18.73[l]
η[g]	0.9	0.9	0.9
α,β,γ [deg][h]	0; 0; 0	10; 6; 0	11; 65; 0
$\lvert D\rvert$ [cm^{-1}][i]	1.6	1.6	2.4
E/D[j]	0.33	0.33	0.33
J [cm^{-1}][k]	−9.7	−11.5	

[a] Local spin at a single Fe site. [b] Ground state. [c] Isomer shift vs. α-Fe at 298 K. [d] Quadrupole splitting; [e] Line width at half-height. [f] Mössbauer hyperfine coupling constants (isotropic part). [g] Asymmetry parameter; [h] Euler angles. [i] Zero-field splitting parameter from susceptibility measurements of **2**. [j] Rhombicity from the EPR spectrum of $[GaFe(bbpo)Cl_4]^{2-}$. [k] Heisenberg coupling constant from susceptibility measurements of **2**. [l] $A_{local} = {}^6/_7\, A_{exp}$.

$[N(n\mathrm{Bu})_4]PF_6$) at a glassy carbon working electrode and an $Ag/AgNO_3$ reference electrode. Ferrocene was used as an internal standard; all potentials are referenced versus the ferrocenium/ferrocene couple (Fc^+/Fc). Figure 5 displays the CVs of **1** (top) and **2** (bottom).

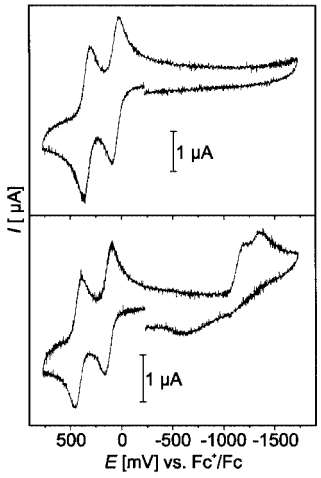

Figure 5. Cyclic voltammograms of **1** (top) and **2** (bottom) in CH_2Cl_2 {0.10 M $[N(n\mathrm{Bu})_4]PF_6$} at 248 K at a scan rate of 100 mV s^{-1} (glassy carbon working electrode; $Ag/AgNO_3$ reference electrode; ferrocene internal standard)

Both **1** and **2** display two reversible one-electron transfer waves in the potential range −0.5 to +0.75 V. The two redox potentials $E^1_{1/2}$ and $E^2_{1/2}$ are observed at +0.077 and +0.354 V for **1**; and at +0.156 and 0.454 V for **2**. Coulometric measurements at appropriately fixed potentials established that both processes correspond to two successive one-electron oxidations of **1** and **2**, respectively, as shown in Equation (2). We will show below that both oxidations are ligand-centered processes that generate the mono- and diradicals $(bbpo^{ox1})^{3-}$ and $(bbpo^{ox2})^{2-}$ shown in Scheme 2.

$$[M^{III}_2(bbpo)Cl_4]^{2-} \underset{+e}{\overset{-e}{\rightleftharpoons}} [M^{III}_2(bbpo)^{ox1\cdot}Cl_4]^{1-} \underset{+e}{\overset{-e}{\rightleftharpoons}} [M^{III}_2(bbpo)^{ox2\cdot-}Cl_4]^{0} \qquad (2)$$
$$E^1_{1/2} \qquad E^2_{1/2}$$

Upon increasing the potential range scanned to −1.7 V the resulting CV of **1** did not show an additional redox process but **2** displayed two successive, irreversible, probably metal-centered reductions: $Fe^{III} \rightarrow Fe^{II}$ at ca. −1.1 and ca. −1.4 V.

Since the coulometric measurements had established that the monoanions, and to a lesser degree the neutral forms of **1** and **2**, are stable in solution their electronic spectra were recorded. The neutral species of **2** proved to be unstable. Figure 6 shows the electronic spectrum of **1** and of its one-electron oxidized form in CH_2Cl_2. As expected, the spectrum of **1** is featureless at $\lambda > 500$ nm but shows an intense absorption at 405 nm (8.6×10^3 M^{-1}·cm^{-1}) which decreases and splits into two bands upon oxidation [393 (7.1×10^3), 412 (7.5×10^3)]. Remarkably, oxidation also yields a broad absorption at 908 nm (730 M^{-1}·cm^{-1}) that is typical for the *o*-iminobenzosemiquinonate(1−) radical.[2]

Electrochemical oxidation the monoanion to the neutral species $[Ga_2(bbpo^{ox2})\ Cl_4]$ is shown in Figure 6 (bottom). Roughly, the absorption maxima of the monoanion double their intensity: 382 sh (7.2×10^3), 402 (8.9×10^3), 414 sh, 421 (9.7×10^3), 466 (3.7×10^3), 506 (2.3×10^3), 727 sh, 874 nm (1.4×10^3 M^{-1}·cm^{-1}), indicating that a second *o*-iminophenolate moiety of the ligand is converted into the corresponding π-radical (Scheme 2). Figure 7 shows the electronic spectra of the di- and monoanions, $[Fe^{III}_2(bbpo)Cl_4]^{2-}$ and $[Fe^{III}_2(bbpo^{ox1})Cl_4]^{-}$, respectively. The spectrum of the dianion displays a typical phenolate-to-iron(III) charge-transfer band at 648 nm (5.0×10^3 M^{-1}·cm^{-1}) and two ligand-based CT bands at 379 (1.5×10^4 M^{-1}·cm^{-1}) and 342 nm (1.7×10^4 M^{-1}·cm^{-1}). The spectrum of the monoanion is similar: 366 sh (1.5×10^4 M^{-1}·cm^{-1}), 406 (1.5×10^4 M^{-1}·cm^{-1}), 492 sh (5.6×10^3 M^{-1}·cm^{-1}), 697 nm (5.0×10^3 M^{-1}·cm^{-1}).

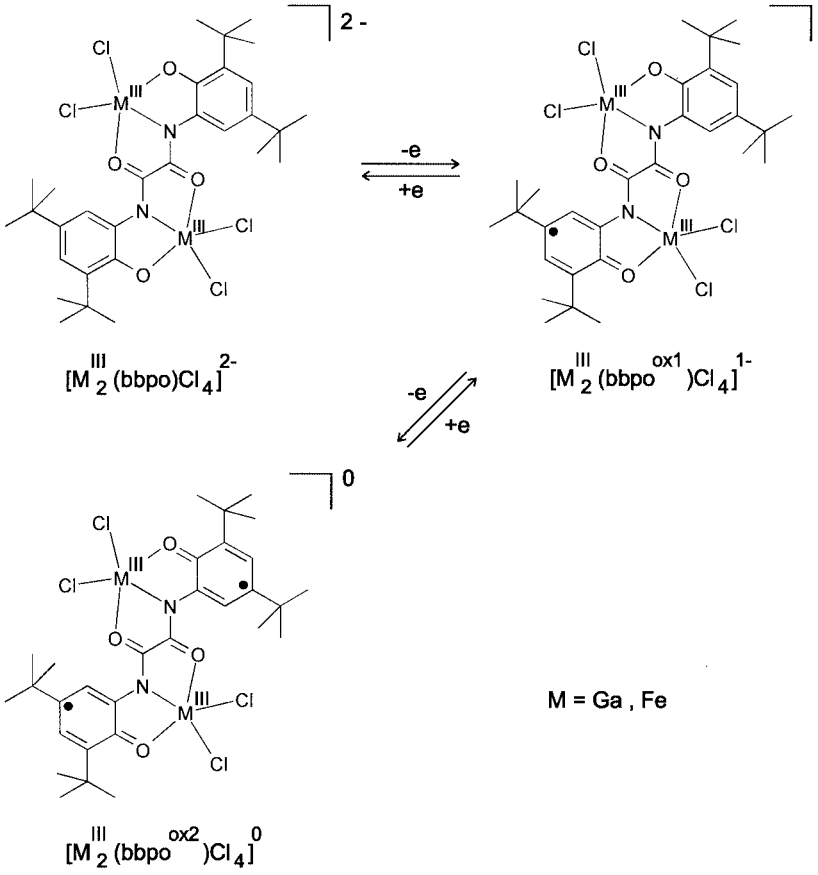

Scheme 2

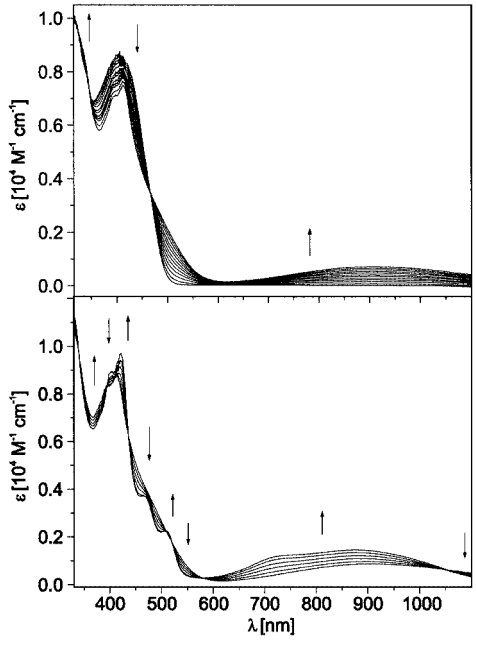

Figure 6. Electronic absorption spectra of **1** and its electrochemically generated one-electron oxidized form (top) at 248 K in CH_2Cl_2 solution {0.10 M $[N(nBu)_4]PF_6$} and of the monoanion and the neutral species (bottom), both of which were electrochemically generated

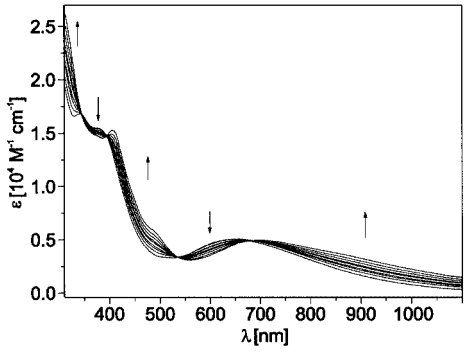

Figure 7. Electronic absorption spectra of **2** and its electrochemically generated one-electron oxidized form at 248 K in CH_2Cl_2 solution {0.10 M $[N(nBu)_4]PF_6$}

2.5. X-band EPR Spectra of *Oxidized* 1 and 2

The X-band EPR spectra of the electrochemically generated monoanion and the neutral complex of **1** have been recorded at 298 K (Figure 8 top and bottom, respectively). Both spectra display typical S = $^1/_2$ signals at g = 2.004 for the monoanion and at g = 2.005 for the neutral species, with clearly discernible Ga hyperfine splitting (I = $^3/_2$) with a_{Ga} = 13.1 MHz for $[Ga_2^{III}(bbpo^{ox1})Cl_4]^{1-}$ and 13.9 MHz

for $[Ga_2^{III}(bbpo^{ox2})Cl_4]^0$. In both cases the unpaired spin couples only to a single Ga nucleus. This indicates that the spin in the monoanion $[Ga_2^{III}(bbpo^{ox1})Cl_4]^-$ is not delocalized over the whole bridging π-radical ligand $(bbpo^{ox1})^{3-}$ but is localized on one *o*-iminobenzosemiquinonato part. There is no or only very weak electronic coupling through the oxamide C−C bond. This notion is nicely corroborated by the EPR spectrum of the neutral species, which shows virtually the same hyperfine pattern as the monoradical and thus clearly indicates that there are two equivalent (*o*-iminobenzosemiquinonato)gallium(III) ($S = {}^1/_2$) units present without significant exchange interaction. Preliminary simulations (not depicted) suggest that the weak line broadening observed for the diradical species might be consistent with a coupling constant of the order $J = 20$ MHz (7×10^{-4} cm^{-1}).

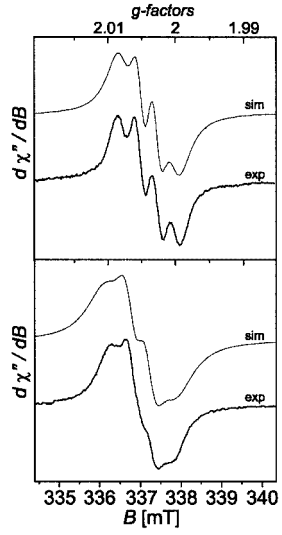

Figure 8. X-band EPR spectra of electrochemically generated monoanion of **1** (top) and of the two-electron oxidized form **1** (bottom) at ambient temperature in fluid solution; simulation parameters are given in the text; conditions: top spectrum (bottom spectrum): frequency 9.4485 GHz (9.4534 GHz); power 7 mW (10 mW); modulation frequency 100 kHz (100 kHz); modulation amplitude 0.08 mT (0.2 mT)

The X-band EPR spectrum of the electrochemically generated monoanion of **2** in frozen CH_2Cl_2 {0.10 M $[N(nBu)_4]PF_6$} at 10 K (Figure 9) clearly establishes that $[Fe_2^{III}(bbpo^{ox1})Cl_4]^-$ possesses an $S_t = {}^1/_2$ ground state since a rhombic signal with $g_x = 1.998$, $g_y = 1.944$, and $g_z = 1.825$ is observed. This $S_t = {}^1/_2$ ground state is assumed to be attained via a relatively strong intramolecular antiferromagnetic coupling, *J*, between an *o*-iminobenzosemiquinonate radical and an high-spin ferric ion, yielding S* = 2, which in turn couples weakly antiferromagnetically to the second high-spin ferric ion, *J′*, as shown in Scheme 3. Electronic coupling between this second ferric ion and the ligand radical is assumed to be either negligibly small or zero.

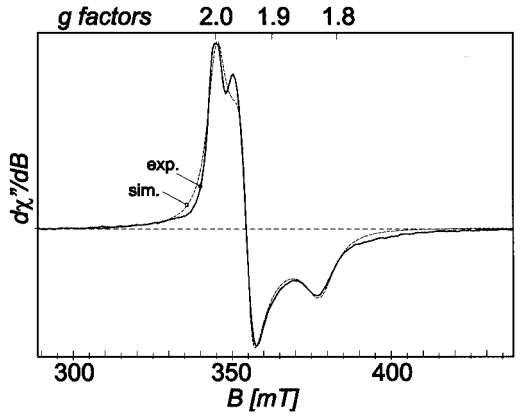

Figure 9. X-band EPR spectrum of electrochemically generated monoanion of **2** in frozen CH_2Cl_2 {0.10 M $[N(nBu)_4]PF_6$} solution at 10 K; the line widths for the simulation are: $W_x = 5.6$; $W_y = 3.4$; $W_z = 13.9$ mT ($g_x = 1.998$; $g_y = 1.944$; $g_z = 1.825$); conditions: frequency 9.6500 GHz; power 100 μW; modulation frequency 100 kHz; modulation amplitude 1.28 mT

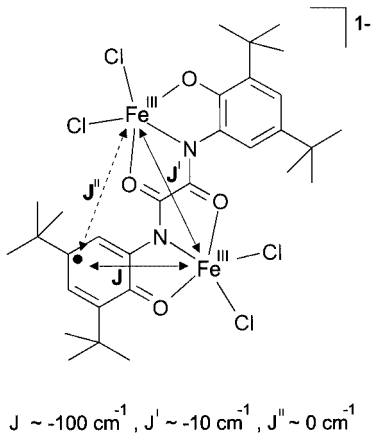

Scheme 3

The *g* values of the $S_t = {}^1/_2$ ground state of oxidized **2** deviate significantly from $g = 2.0$, in contrast to what can be expected from the single-ion properties of the ^6S state of high-spin Fe^{III} or a ligand radical. This does *not* necessarily indicate the formation of Fe^{IV}; the large *g* shifts owe their origin to level mixing of the ground state doublet with excited quadruplet due to competing exchange and ZFS, similar to what was found for **2**. This situation resembles moderately strong coupled high-spin Fe^{III}/Fe^{II} dimers ($S_1 = {}^5/_2$, $S_2 = 2$) as found in the OH-bridged diiron cores of purple-acid phosphatases, methane monooxygenase, and related model compounds[10] where the *g* values span the large range 1.5−2. We achieved a quantitative interpretation of the *g* values of oxidized **2** from a corresponding spin-Hamiltonian approach based on the simplified coupling scheme shown in Scheme 3 by using Equation (1) with $S_1 = {}^5/_2$ for an Fe^{III} site and a fictitious spin $S_2 = S^* = 2$. The latter is the spin of the pair formed by one iron(III) and the very strongly coupled ligand π-radical. This allowed us to probe the effect of ligand oxidation on the electronic properties of

the respective Fe^{III} site even if their spin coupling is too strong to measure. A reasonable fit of the experimental *g* values was obtained with $D_1 = 1.6\ cm^{-1}$, $E/D_1 = 0.33$ (fixed to the values taken from nonoxidized **2**) and $D_2 = 2.4\ cm^{-1}$, $E/D_2 = 0.33$ (fixed), and $J = -11.5\ cm^{-1}$. (We refrained from introducing local g anisotropies or Euler rotations of the principal axes systems.) The values of D_2 and *J* are convincingly close to what is obtained theoretically for *unperturbed* iron sites by converting the local values of non-oxidized **2** into the oxidized system with $S_2 = S^* = S_{Fe} + S_{rad}$ using spin projection techniques[11]: $D_2 = 2.13\ cm^{-1}$ ($= {}^4/_3\ D_{Fe}$). $E/D_2 = 0.33$, $J = -11.3\ cm^{-1} = {}^7/_6\ J$ ($S_1 = {}^5/_2$, $S_2 = {}^5/_2$). Hence, the unusual EPR *g* values of oxidized **2** are fully consistent with the concept of ligand oxidation and the simplified coupling scheme for the spin ground state with "infinitively" strong Fe^{III}−radical coupling.

2.6. Mössbauer Spectra of *Oxidized* 2

The zero- and applied-field Mössbauer spectra of oxidized **2** were obtained by using the following protocol. The monoanion of **2** was generated coulometrically in CH_2Cl_2 solution {0.10 M $[N(nBu)_4]PF_6$} at 248 K and then frozen to 80 K and transferred to a Mössbauer cup. Subsequently, the solvent CH_2Cl_2 was removed by evaporation under reduced pressure at −30 °C within 2 h and then the sample was rapidly cooled to 80 K. In a parallel experiment the remaining solution was monitored at −30 °C spectrophotometrically to check the redox stability of the monoanion. No decomposition was detected after 2 h.

The zero-field spectrum of $[Fe_2^{III}(bbpo^{ox1})Cl_4]^-$ displays a broad doublet ($\Gamma = 0.82\ mm{\cdot}s^{-1}$, not shown) that could be fitted with two slightly different quadrupole doublets of two non-equivalent ferric sites. The isomer shift and quadrupole splitting parameters of both doublets are similar and are nearly identical to those observed for the dianion (see above). This implies that the one-electron oxidation of **2** is a ligand-centered process. No indication for the presence of Fe^{IV} has been found.

It is interesting and instructive that the applied-field spectra of the monoanion (Figure 10) are significantly more complex than the spectra recorded for the symmetrical dinuclear complex **2** (Figure 4). The magnetic spectra of the monoanion display very broad signals over a large velocity range of ca. $10\ mm{\cdot}s^{-1}$ whereas the analogous spectra of **2** cover only ca. $3\ mm{\cdot}s^{-1}$. The latter were simulated with a single high-spin ferric site, which is definitely not possible for the spectra of the monoanion. Here, the two ferric ions are nonequivalent. We have used the spin coupling Scheme outlined above (and shown in Scheme 3) for the monoanion of **2** where the $S_t = {}^1/_2$ ground state is attained by a strong coupling between one high-spin ferric ion and a ligand π-radical, yielding a fictitious local S* = 2 spin state and, in addition, a weak coupling of this state with the second high-spin ferric ion.

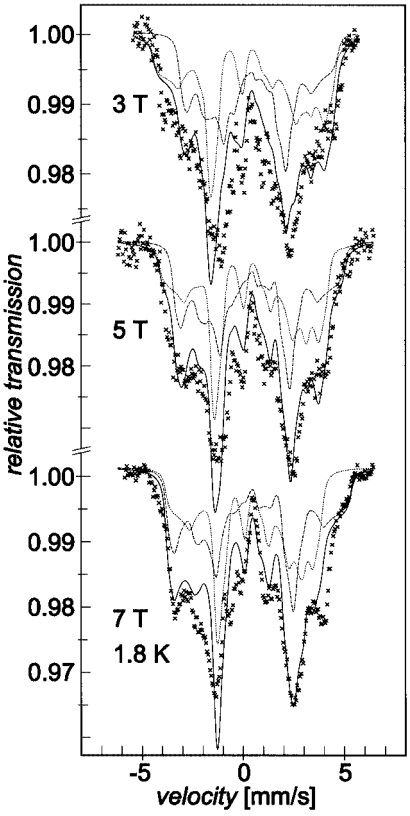

Figure 10. Applied-field Mössbauer spectra of electrochemically generated monoanion of **2** after removal of the solvent CH_2Cl_2 under reduced pressure; simulation parameters are given in Table 3; experimental data are corrected for residual non-oxidized compound **2** by subtracting 10% of the species shown in Figure 4

The same electronic Hamiltonian [Equation (1)] was applied as for the EPR interpretation of oxidized **2**, and the ZFS parameters were taken from the EPR results. Isomer shift, quadrupole splitting, asymmetry parameter and (isotropic) *A* constant of the ferric site could be taken from the data of the diferric starting complex **2**, whereas those of the oxidized S* = 2 site were independently optimized. The results are summarized in Table 3. The experimental *A* value obtained for S* = 2 was converted into a local value for Fe^{III}, $S = {}^5/_2$ by using $A_{Fe} = {}^6/_7\ A_{S^*=2}$.

It is remarkable that the quadrupole splitting and isomer shift of the ferric site with the ligand radical are slightly increased with respect to those of the starting compound or the other ferric site of oxidized **2**, whereas the local hyperfine coupling constant is significantly decreased. Similar systematic trends were indicated previously for the oxidation of iron(III) complexes with phenolate ligands.[12] The variation of the quadrupole splitting (which has no valence contribution for the $3d^5$ configuration) and the increase of the isomer shift reflect the attenuated π-donor capability of the oxidized ligand. The lower covalency of the iron−π-radical bonds for one iron site appears to be the origin of the slight increase of the iron−iron exchange coupling. The reduction of local hyperfine coupling of the ^{57}Fe nucleus at

the "oxidized" iron site originates from covalent delocalization of radical β-spin density into the α-spin carrying metal d orbitals. The effect corresponds to spin density delocalization onto the central metal ion in radical complexes with *diamagnetic* central ions for which relative strong super hyperfine coupling with the metal nuclei is observed in the EPR spectra. Among others, oxidized compound **1** represents such an example.[1−6] The mechanism of spin delocalization corresponds to that of "*transferred*" or "*super-transferred hyperfine field*" described in solid-state applications of Mössbauer spectroscopy and magnetic materials.[13]

Conclusion

We have shown here that the tetraanion of 1,2-bis(3,5-di-*tert*-butyl-2-hydroxyphenyl)oxamide is a redox-noninnocent dinucleating ligand that reacts with 2 equiv. of $GaCl_3$ or $FeCl_3$ to form the dianionic complexes $[Ga^{III}_2(bbpo)Cl_4]^{2-}$ and $[Fe^{III}_2(bbpo)Cl_4]^{2-}$, respectively. Both dianions undergo, electrochemically, two reversible one-electron oxidations, yielding the monoanions $[M^{III}_2(bbpo^{ox1})Cl_4]^-$ (M = Ga^{III},Fe^{III}) and the neutral species $[M^{III}(bbpo^{ox2})Cl_4]^0$, respectively. The trianion $(bbpo^{ox1})^{3-}$ is a π-radical ($S = {}^1/_2$) whereas the dianion $(bbpo^{ox2})^{2-}$ is a diradical, both of which are of the *o*-iminobenzosemiquinonate type.

The three-spin system of the monoanion $[Fe^{III}_2(bbpo^{ox1})Cl_4]^-$ can be described by a ligand π-radical that couples strongly antiferromagnetically to a high-spin ferric ion, yielding a fictitious S* = 2 state, which in turn couples weakly antiferromagnetically to a second high-spin ferric ion to yield the observed $S_t = {}^1/_2$ ground state. The monoanion $[Ga^{III}_2(bbpo^{ox1})Cl_4]^-$ possesses an $S = {}^1/_2$ ground state whereas the neutral species displays, at room temperature, two uncoupled (*o*-iminobenzosemiquinonate)-gallium(III) units that couple antiferromagnetically at very low temperatures, yielding an $S_t = 0$ ground state. The spin structure provides interesting magnetic properties of long-range coupled systems with competing interactions.

Experimental Section

1,2-Bis(3,5-di-*tert*-butyl-2-hydroxoyphenyl)oxamide [H_4(bbpo)]: To an argon-purged suspension of 2-amino-4,6-di-*tert*-butylphenol[7] (4.4 g, 20 mmol) and triethylamine (2.0 g, 20 mmol) in dry diethyl ether (50 mL), oxalyl chloride (1.3 g, 10 mmol) was added dropwise at 0 °C. After stirring at 0 °C for 30 min, stirring was continued for further 2 h at 20 °C. The resultant colorless precipitate was filtered off and washed with diethyl ether. To the residue was added H_2O (20 mL) and the ligand H_4(bbpo) was filtered off and washed with H_2O until the water was free of chloride. A yellowish powder (3.0 g, 61%) was obtained which was stored under Ar; m.p. 217 °C (uncorrected). ^{1}H NMR (400 MHz, $CDCl_3$, 300 K): δ = 1.29 (s, 18 H, *tert*-butyl), 1.44 (s, 18 H, *tert*-butyl), 7.11 (m, 2 H, *p*-H), 7.28 (m, 2 H, *o*-H), 7.49 (s, 2 H, OH), 9.49 (s, 2 H, NH) ppm. ^{13}C{H} (63 MHz, $CDCl_3$, 300 K): δ = 29.8, 31.4, 34.4, 35.4, 117.7, 123.1, 124.0, 139.7, 143.3, 145.8, 157.2 ppm. MS (EI): *m*/*z* = 496. IR (KBr): $\tilde{\nu}$ = 3342 ν(N−H), 3140 ν(O−H), 1655, 1603, 1530 ν(C=O), ν(C−N) cm^{-1}. $C_{30}H_{44}N_2O_4$ (496.69): calcd. C 72.55, H 8.93, N 5.64; found C 72.8, H 8.7, N 5.4.

[N(*n*Bu)$_4$]$_2$[Ga^{III}_2(bbpo)Cl$_4$] (1): To an argon-purged suspension of the ligand H_4(bbpo) (0.50 g, 1.0 mmol) in dry CH_3OH (20 mL), was added NaOH (2 mL, 1.0 M in CH_3OH). An argon-purged solution of $GaCl_3$ (0.36 g, 2.0 mmol), dissolved in 2−3 mL of CH_3OH was added and upon continuous stirring at 20 °C a yellow precipitate formed. The mixture was then heated to reflux under Ar and [N(*n*Bu)$_4$]Cl (0.56 g, 2.0 mmol) was added. After heating to reflux for a further 4 h, a yellow, microcrystalline precipitate of **1** was obtained. Yield 0.66 g (55%). Recrystallization from CH_3OH solution by diethyl ether diffusion yielded single crystals of **1** suitable for X-ray analysis. $C_{62}H_{112}Cl_4Ga_2N_4O_4$ (1258.85): calcd. C 59.16, H 8.97, Cl 11.27, Ga 11.08, N 4.45; found C 60.0, H 8.7, Cl 11.1, Ga 11.3, N 4.6. MS (ESI-neg. ion): *m*/*z* = 737.1 $\{[Ga_2(bbpo)Cl_3]\}^-$. ^{1}H NMR (250 MHz, [D_4]MeOD, 300 K): δ = 1.02 [t, 24 H, CH_3(TBA)], 1.29 (s, 18 H, *tert*-butyl), 1.40 [m, 16 H, CH_2(TBA)], 1.47 (s, 18 H, *tert*-butyl), 1.65 [m, 16 H, CH_2(TBA)], 3.23 [t, 16 H, CH_2(TBA)], 7.13 (d, ^4J = 2.3 Hz, 2 H), 8.04 (d, ^4J = 2.4 Hz, 2 H) ppm.

[N(*n*Bu)$_4$]$_2$[Fe^{III}_2(bbpo)Cl$_4$] (2): This iron-containing complex was prepared in the same fashion as described above for the synthesis of **1** but using $FeCl_3$ instead of $GaCl_3$. The green microcrystalline product was recrystallized from CH_3OH by diethyl ether diffusion, yielding single crystals of **2** suitable for X-ray crystallography. $C_{62}H_{112}Cl_4Fe_2N_4O_4$ (1231.10): calcd. C 60.49, H 9.17, Cl 11.52, Fe 9.07, N 4.55; found C 60.5, H 9.1, Cl 11.4, Fe 9.1, N 4.6. MS (ESI-neg. ion): *m*/*z* = 709.1.

X-ray Crystallographic Data Collection and Refinement of the Structures: A yellow single crystal of **1** and a black crystal of **2** were coated with perfluoropolyether, picked up with a glass fiber and mounted in the nitrogen cold stream of the diffractometer. Intensity data were collected at 100 K using graphite-monochromated Mo-K_α radiation (λ = 0.71073 Å). The final cell constants were obtained from a least-squares fit of a subset of several thousand strong reflections. Data collection was performed by taking frames at 1.0° (Nonius Kappa-CCD) in ω. Crystallographic data of the compounds are listed in Table 1. The Siemens ShelXTL software package was used for solution, refinement and artwork of the structure.[14,15] The structures were readily solved by direct methods and difference Fourier techniques. All non-hydrogen atoms and hydrogen atoms were placed at calculated positions and refined as riding atoms with isotropic displacement parameters. Split-atom models with restrained C−C distances using the SADI option in SHELX97 were introduced in both structures to account for their disorder by rotation. CCDC-191601 (**1**) and -191602 (**2**) contain the supplementary crystallographic data for this paper. These data can be obtained free of charge at www.ccdc.cam.ac.uk/conts/retrieving.html or from the Cambridge Crystallographic Data Centre, 12 Union Road, Cambridge CB2 1EZ, UK [Fax: (internat.) + 44-1223/336-033; E-mail: deposit@ccdc.cam.ac.uk].

Physical Measurements: Electronic spectra of complexes and spectra of the spectroelectrochemical measurements were recorded with an HP 8452A diode array spectrophotometer (range: 190−1100 nm). Cyclic and square-wave voltammograms and coulometric experiments were performed with an EG&G potentiostat/galvanostat. Temperature-dependent (2−298 K) magnetization data were recorded with a SQUID magnetometer (MPMS Quantum design) in an external magnetic field of 1 T. The experimental susceptibility data were corrected for underlying diamagnetism by use of tabulated Pascal's constants. X-band EPR spectra were re-

corded with a Bruker ESP 300 spectrometer. Zero- and applied-field Mössbauer spectra were recorded using the equipment described in ref.[16]; programs used for fitting routines have also been described.

Acknowledgments

We thank the Fonds der Chemischen Industrie for financial support.

[1] C. N. Verani, S. Gallert, E. Bill, T. Weyhermüller, K. Wieghardt, P. Chaudhuri, *Chem. Commun.* **1999**, 1747.
[2] P. Chaudhuri, C. N. Verani, E. Bill, E. Bothe, T. Weyhermüller, K. Wieghardt, *J. Am. Chem. Soc.* **2001**, *123*, 2213.
[3] H. Chun, C. N. Verani, P. Chaudhuri, E. Bothe, E. Bill, T. Weyhermüller, K. Wieghardt, *Inorg. Chem.* **2001**, *40*, 4157.
[4] H. Chun, T. Weyhermüller, E. Bill, K. Wieghardt, *Angew. Chem.* **2001**, *113*, 2552; *Angew. Chem. Int. Ed.* **2001**, *40*, 2489.
[5] X. Sun, H. Chun, K. Hildenbrand, E. Bothe, T. Weyhermüller, K. Wieghardt, *Inorg. Chem.* **2002**, *41*, 4295.
[6] H. Chun, P. Chaudhuri, T. Weyhermüller, K. Wieghardt, *Inorg. Chem.* **2002**, *41*, 790.
[7] V. B. Vol'eva, T. I. Prokof'eva, A. I. Prokov'ef, I. S. Belostotskaya, N. L. Komissarova, V. V. Ershov, *Russ. Chem. Bull.* **1995**, *44*, 1720.
[8] D. Armentano, G. DeMunno, J. Faus, F. Lloret, M. Julve, *Inorg. Chem.* **2001**, *40*, 655.
[9] R. D. Shannon, *Acta Crystallogr., Sect. A* **1976**, *32*, 751.
[10] [10a] J. H. Rodriguez, H. Ok, Y.-M. Xia, P. G. Debrunner, B. E. Hinrichs, T. Meyer, N. H. Packard, *J. Phys. Chem.* **1996**, *100*, 6849−6862. [10b] U. Bossek, H. Hummel, T. Weyhermüller, E. Bill, K. Wieghardt, *Angew. Chem.* **1995**, *107*, 2885−2888.
[11] A. Bencini, D. Gatteschi, *EPR of Exchange Coupled Systems*, Springer Verlag, Berlin, **1990**.
[12] M. D. Snodin, L. Ould-Moussa, U. Wallmann, S. Lecomte, V. Bachler, E. Bill, H. Hummel, T. Weyhermüller, P. Hildebrandt, K. Wieghardt, *Chem. Eur. J.* **1999**, *5*, 2554−2565.
[13] F. Granjean, in *Mössbauer Spectroscopy Applied to Inorganic Chemistry* (Ed.: G. J. Long), Plenum Press, New York, **1987**, vol. 2, p. 241−271.
[14] G. M. Sheldrick, Universität Göttingen, **1994**.
[15] ShelXTL V.5, Siemens Analytical X-ray Instruments, Inc., **1994**.
[16] K. Meyer, E. Bill, B. Mienert, T. Weyhermüller, K. Wieghardt, *J. Am. Chem. Soc.* **1999**, *121*, 4859.

Received September 25, 2002

